Plasmonic modes in nanowire dimers: A study based on the hydrodynamic Drude model including nonlocal and nonlinear effects

Matthias Moeferdt,[1] Thomas Kiel,[1] Tobias Sproll,[2] Francesco Intravaia,[2] and Kurt Busch[1,2]

[1]*AG Theoretische Optik & Photonik, Institut für Physik, Humboldt-Universität zu Berlin, 12489 Berlin, Germany*
[2]*Max-Born-Institut, 12489 Berlin, Germany*

A combined analytical and numerical study of the modes in two distinct plasmonic nanowire systems is presented. The computations are based on a discontinuous Galerkin time-domain approach, and a fully nonlinear and nonlocal hydrodynamic Drude model for the metal is utilized. In the linear regime, these computations demonstrate the strong influence of nonlocality on the field distributions as well as on the scattering and absorption spectra. Based on these results, second-harmonic-generation efficiencies are computed over a frequency range that covers all relevant modes of the linear spectra. In order to interpret the physical mechanisms that lead to corresponding field distributions, the associated linear quasielectrostatic problem is solved analytically via conformal transformation techniques. This provides an intuitive classification of the linear excitations of the systems that is then applied to the full Maxwell case. Based on this classification, group theory facilitates the determination of the selection rules for the efficient excitation of modes in both the linear and nonlinear regimes. This leads to significantly enhanced second-harmonic generation via judiciously exploiting the system symmetries. These results regarding the mode structure and second-harmonic generation are of direct relevance to other nanoantenna systems.

I. INTRODUCTION

Nanoplasmonic structures lie at the heart of numerous recent advances in different research areas of fundamental physics and technological applications. Examples include surface- and tip-enhanced Raman scattering, frequency conversion, nanoantennas, metasurfaces, and hyperbolic metamaterials. While in many cases the modeling of the metallic elements via linear Drude or Drude-Lorentz models is sufficient, a number of scenarios exist where more refined material models are required. These scenarios include structures with nanoscale features such as nanogaps, tips, and grooves as well as nanoantennas with emitters in their respective near field for which taking into account the spatially nonlocal and/or nonlinear characteristics of the metals is necessary for an accurate description of the system. As a result, corresponding advanced materials models, specifically the hydrodynamic Drude model and various extensions thereof, have recently received considerable attention [1–20]. For instance, the hydrodynamic Drude model allows us to investigate the frequency shifts, the excitation of bulk plasmons, nonlinear wave-mixing phenomena such as second-harmonic generation, and modified field distributions and intensities. While it has been argued that, in the linear regime, the hydrodynamic model yields only semiquantitative results [8], recent improvements regarding refined treatments of the systems' behavior at interfaces [13,14], as well as the incorporation of interband transitions [2,13] and Landau damping [3,10], have demonstrated that fully quantitative results may be obtained nonetheless [13].

Numerical computations using the hydrodynamic Drude model are more demanding than those employing the ordinary Drude model. In particular, the description of the interfaces' behavior as well as of the potential constraining the electronic fluid, needed for an adequate resolution of bulk plasmons with a typical wavelength of the order of 1 nm, requires very efficient Maxwell solvers. In recent years, new numerical schemes for solving the hydrodynamic equations in a nonperturbative fashion have emerged [17,21]. In contrast to earlier works [6,7], time-domain approaches provide direct access to the nonlinear properties of the hydrodynamic Drude model by solving the full set of nonlinear equations [17,18,21], without making any further assumptions about the nonlinear source terms. In particular, the discontinuous Galerkin time-domain (DGTD) method [22], a time-dependent finite-element framework, has shown good performance characteristics for both nonlocal and nonlinear properties [17,23].

In this work, we utilize the DGTD approach to investigate the hydrodynamic Drude model. Specifically, we discuss both its nonlocal and nonlinear characteristics by employing a cylindrical nanowire dimer system and a single V-groove structure as illustrative examples. The cylindrical dimer is a particularly interesting system to study: Indeed, despite its low symmetry, it can be treated analytically within a (quasi)electrostatic approach. This allows, in turn, employing a conformal transformation which provides a quite useful classification of the modes existing in the system (see Sec. II). These analytical results are subsequently utilized to accurately interpret the numerical outcomes (Sec. III). Our first key finding is that, for a specific angle of incidence, the spatial nonlocality has a particularly strong effect on the scattering spectra. Second, we demonstrate that, due to the nonlinearity, modes are efficiently excited via second-harmonic generation (SHG), while in the linear regime their excitation is symmetry suppressed. In addition, our group-theoretical considerations
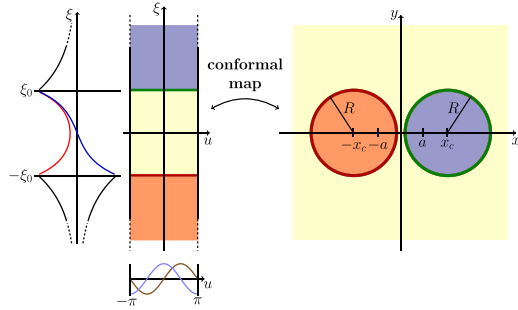
FIG. 1. Conformal map for bicylindrical coordinates. The colors indicate which regions are mapped onto each other. The cylindrical structure imposes a 2π periodicity on the u coordinate. The solutions for the electrostatic potential as functions of the bicylindrical coordinates ξ and u are therefore given by trigonometric and hyperbolic functions (displayed on the left).

allow us to discuss SHG efficiencies by properly tuning the modes into singly and doubly resonant conditions. These key findings are directly applicable to more general nanoantenna structures.

II. QUASIELECTROSTATIC THEORY OF A CYLINDRICAL NANOWIRE DIMER

We consider two identical, parallel, and infinitely extended circular nanowires with a 10-nm radius, separated by a 2-nm gap. These wires are situated in vacuum and are made of a Drude metal, described by a (local and linear) dielectric constant

$$\epsilon(\omega) = 1 - \frac{\omega_p^2}{\omega(\omega + i\gamma)}, \qquad (1)$$

with a plasma frequency $\omega_p = 1.39 \times 10^{16}$ rad/s ($\sim$9 eV) and damping constant $\gamma = 3.23 \times 10^{13}$ rad/s ($\sim$21 meV). These values correspond to the Drude contribution to the permittivity of silver reported by Johnson and Christy [24]. With these parameters the system can be described to a good approximation within the quasielectrostatic approximation, which amounts to neglecting retardation effects and setting the speed of light to infinity. In the quasielectrostatic limit, the dimer structure can be treated analytically. This is done by performing a conformal map to an appropriate coordinate system, where the Laplace equation, which in quasielectrostatics takes over the role of the wave equation, becomes separable [25–27]. The mapping, which describes a transformation between a strip of $\mathbb{R}^2$ and two cylinders, is depicted schematically in Fig. 1. The corresponding bicylindrical coordinates are called ξ and u, and the transformation from the Cartesian coordinates reads

$$x = \frac{a \sinh \xi}{\cosh \xi - \cos u}, \quad y = \frac{a \sin u}{\cosh \xi - \cos u}. \qquad (2)$$

The system is built around two foci which lie at $x = \pm a$. The parameter a depends on the parameters characterizing the system we wish to describe and is uniquely determined for a specific set of radii $R_{1,2}$ and center points $x_{c_{1,2}}$ of the cylinders by the following relations [25]:

$$x_{c_{1,2}} = \frac{a}{\tanh \xi_{1,2}}, \quad R_{1,2} = \frac{a}{|\sinh \xi_{1,2}|}. \qquad (3)$$

The ξ-level lines are nonconcentric circles (so-called Apollonian circles) around the foci, which lie in the left half-space ($x < 0$) for $\xi < 0$ and in the right half-space ($x > 0$) for $\xi > 0$. For $\xi \to \pm\infty$ the circles collapse into the foci, and for $\xi \to 0$ they enclose the corresponding half-space ($x > 0$ for $\xi \to 0^+$ or $x < 0$ for $\xi \to 0^-$) and the entire y axis. The vacuum-metal interfaces where the boundary conditions for the fields have to be imposed are thus given by two fixed ξ-level lines, $\xi = \xi_{1,2}$. In the present case, we consider cylinders with equal radii $R_{1,2} = R = 10$ nm and a gap of 2 nm, corresponding to $x_{c_{1,2}} = \pm x_c = \pm 11$ nm. We then have

$$\xi_{1,2} = \pm\xi_0 = \pm\operatorname{arcosh}\left(\frac{x_c}{R}\right) = \pm 0.443568245\ldots, \qquad (4)$$

$$a = 4.582575\ldots \text{ nm}. \qquad (5)$$

Within these coordinates, the Laplace equation reads

$$\Delta V = \left(\frac{\cosh \xi - \cos u}{a}\right)^2 \left[\partial_\xi^2 V + \partial_u^2 V\right] = 0. \qquad (6)$$

This equation is separable and has the harmonic solutions

$$V_1 = [\sinh m\xi, \cosh m\xi] \quad \text{or} \quad [e^{m\xi}, e^{-m\xi}], \qquad (7)$$

$$V_2 = [\sin mu, \cos mu] \qquad \text{or} \quad [e^{imu}, e^{-imu}], \qquad (8)$$

which are depicted along with the mapping in Fig. 1. From this, we can construct four physical solutions as combinations of u and ξ, where the variable u plays the role of the azimuthal coordinate and introduces a 2π periodicity which results in a "quantization" of the solutions labeled by the discrete index $m \in \mathbb{N}^+$.

In the quasielectrostatic description the electromagnetic boundary conditions read

$$V_i(\pm\xi_0) = V_o(\pm\xi_0),$$
$$\epsilon(\omega)\frac{\partial V_i}{\partial \xi}\bigg|_{\pm\xi_0} = \frac{\partial V_o}{\partial \xi}\bigg|_{\pm\xi_0}, \qquad (9)$$

where the subscripts i and o stand for inside and outside the cylinder, respectively. The permittivity on the inside is given by Eq. (1). The hyperbolic functions of Eqs. (7) are chosen to describe the field outside the cylinders, while exponentially decaying solutions characterize the field inside the cylinder (see Fig. 1).

As a consequence, the composite solutions exhibit different symmetry properties, and we categorize them in four classes (labeled I–IV). The solutions for the potentials and those for the resulting electric field distributions are displayed in Figs. 2 and 3.

The four classes of potentials from Fig. 2 can be identified with the four irreducible representations of the dihedral symmetry point group D_2 (in two dimensions, D_2 is isomorphic to the group C_{2v}) [28,29]. There are four symmetry operations in this group, all of which map the original dimer geometry onto itself: The identity operation I, a rotation around the z axis by 180° C_{2z}, mirroring on the xz plane σ_{xz}, and mirroring on the yz plane σ_{xz}. The group is Abelian and the character table of D_2 is presented in Table I.
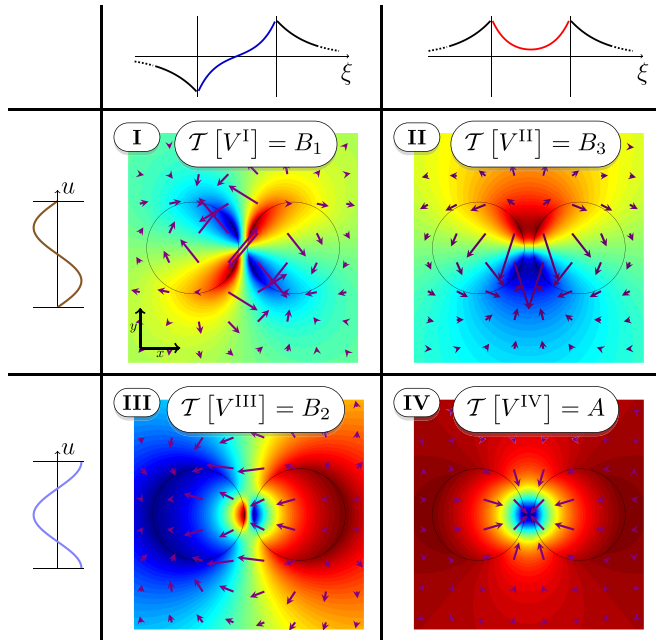
FIG. 2. The harmonic solutions for the electrostatic potential in a bicylindrical setup allow for four classes of solutions with different symmetries. The potentials for $m = 1$ are displayed for each solution; the arrows depict the gradients of the potentials. For each potential, the irreducible representation is given.
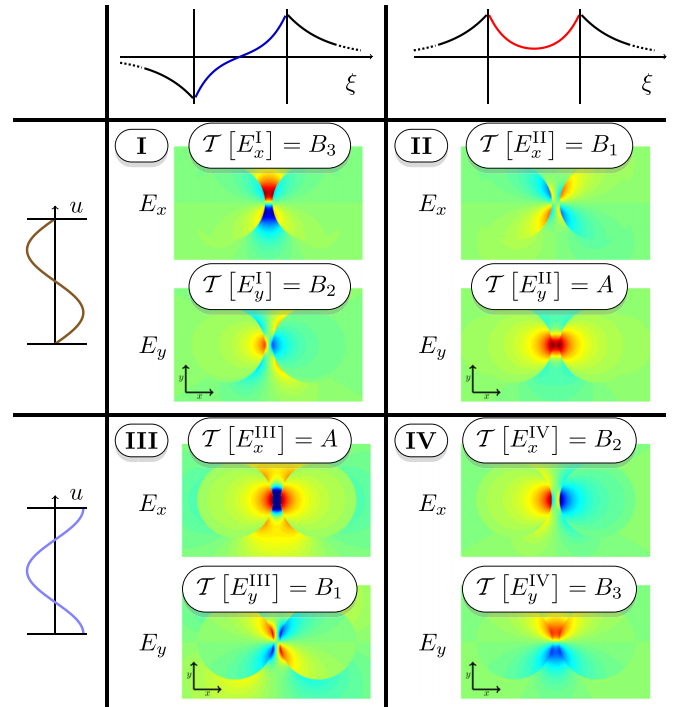

FIG. 3. Electric field distributions for the $m = 1$ modes pertaining to the four symmetry classes. For each field component, the irreducible representation is given. The field components were calculated directly from the potentials in Fig. 2 via $\mathbf{E} = -\nabla V$.

Consequently, the four potentials transform according to

$$\mathcal{T}[V^{\mathrm{I}}] = B_1, \quad \mathcal{T}[V^{\mathrm{II}}] = B_3,$$
$$\mathcal{T}[V^{\mathrm{III}}] = B_2, \quad \mathcal{T}[V^{\mathrm{IV}}] = A, \tag{10}$$

where $\mathcal{T}[F]$ denotes the decomposition of a quantity F into irreducible representations; that is, it indicates under which transformation F is mapped onto itself. The two-dimensional nabla operator transforms as

$$\mathcal{T}[\nabla] = \begin{pmatrix} \mathcal{T}[\partial_x] \\ \mathcal{T}[\partial_y] \end{pmatrix} = \begin{pmatrix} B_2 \\ B_3 \end{pmatrix}. \tag{11}$$

The multiplication rules can be readily extracted from the character table by multiplying the elements in the same column and identifying the results with one of the four possible symmetry classes. By applying the nabla operator to the potentials

$$\mathcal{T}[\nabla]\mathcal{T}[V^i] = \mathcal{T}[\mathbf{E}^i], \quad i = \mathrm{I}, \ldots, \mathrm{IV}, \tag{12}$$

we obtain the symmetries of the fields in Fig. 3, which are not equivalent to the symmetries of the potentials from the same class:

$$\mathcal{T}[\mathbf{E}^{\mathrm{I}}] = \begin{pmatrix} B_3 \\ B_2 \end{pmatrix}, \quad \mathcal{T}[\mathbf{E}^{\mathrm{II}}] = \begin{pmatrix} B_1 \\ A \end{pmatrix},$$
$$\mathcal{T}[\mathbf{E}^{\mathrm{III}}] = \begin{pmatrix} A \\ B_1 \end{pmatrix}, \quad \mathcal{T}[\mathbf{E}^{\mathrm{IV}}] = \begin{pmatrix} B_2 \\ B_3 \end{pmatrix}. \tag{13}$$

In order to excite one of the modes, the irreducible representation of the electric fields of an incoming light pulse has to match those of the field components in Eq. (13). A static external field (as one would have within a capacitor) is represented by A. As a consequence, a static electric field in the x direction is capable of exciting the mode from class II, and a static field in the y direction is capable of exciting that of class III.

By inspection, one finds that the electric field $\mathbf{E}^{k_x}$ of a wave packet propagating in the x direction, with an electric field in the y direction, is represented by

$$\mathcal{T}[E^{k_x}] = A \oplus B_2, \tag{14}$$

where the direct-sum symbol $\oplus$ indicates that the symmetries of the field are given by a superposition of two irreducible representations. In this sum, all signs and magnitudes are dropped. Note, however, that the deeper we enter the quasielectrostatic limit (smaller particle sizes), the smaller the influence of the B_2 contribution on the spectra becomes. The type of excitation given by Eq. (14) complies with the symmetries of modes II and I.

TABLE I. Character table of the Abelian point group D_2 [28].

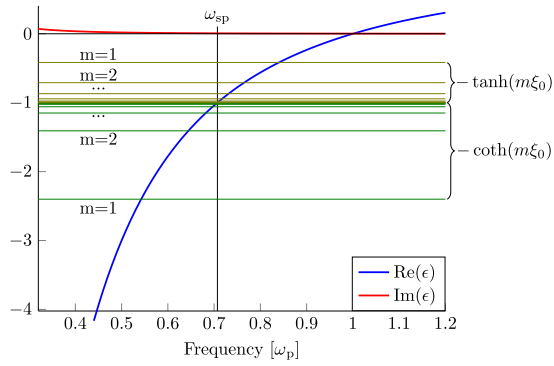| D_2	I	$C_2(z)$	σ_{xz}	σ_{yz}
A	1	1	1	1
B_1	1	1	-1	-1
B_2	1	-1	1	-1
B_3	1	-1	-1	1

FIG. 4. Graphic solution for the electrostatic problem for the cylindrical dimer (neglecting the imaginary part of the permittivity). We find a hybridization of the solutions. For large m, the modes tend to the surface plasmon frequency ω_{sp}.

On the other hand, for a pulse propagating in the y direction with an electric field in the x direction, we have an electric field

$$\mathcal{T}[E^{k_y}] = A \oplus B_3. \tag{15}$$

This field therefore excites modes of classes I and III (see Fig. 3). Thus, modes of class IV are dark for wave packages of this type or linear combinations thereof, i.e., regardless of the angle of incidence.

Having discussed the symmetries of the modes, we proceed to the determination of their frequencies. In the quasielectrostatic problem, the frequency dependence is introduced by means of the material model and the boundary conditions given by Eq. (9). In these considerations, the azimuthal variable u does not play a role because the angular dependence is the same everywhere in space. Therefore, within the quasielectrostatic theory, classes I and III as well as classes II and IV are degenerate. As a result, we arrive at the following solutions:

$$\epsilon(\omega) = -\coth(m\xi_0),$$
$$\epsilon(\omega) = -\tanh(m\xi_0) \tag{16}$$

for solutions I and III and solutions II and IV, respectively, which are displayed in Fig. 4. (The imaginary part of the permittivity is neglected in the graphical solution, but it is included in the analytical calculation of the mode frequencies). The degeneracy is lifted when we go beyond the quasielectrostatic limit. As demonstrated in Fig. 4, for a cylindrical dimer we find a hybridization of modes, having frequencies both below and above that of a single cylinder; namely, the surface plasmon frequency $\omega_{\text{sp}} = \omega_p/\sqrt{2}$, which is obtained from $\text{Re}(\epsilon) = -1$. The modes for $m = 1$ are well separated from the next higher modes. For large m, the mode frequencies tend to ω_{sp}. For infinite separation, $x_c \to \infty$ the mode frequencies collapse to ω_{sp}, and the field distributions become the well-known multipolar distributions of regular cylinders, with their dipoles oriented according to the symmetries described above.

III. NUMERICAL RESULTS

A. Cylindrical dimer

The hydrodynamic model describes the electrons in the metal as a charged and compressible fluid subject to elec-

tromagnetic forcing, leading to a set of equations of motion comprising the Euler equation and the equation of charge conservation. The full electromagnetic problem is then defined by the solution of the dynamics of this system along with the Maxwell equations that couple to the fluid equations via the electric current. We employ the usual hard-wall slip boundary condition, which consists of setting the normal component of the fluid's velocity to zero at the material surface, allowing the electrons to slip sideways [30]. This additional boundary condition (of nonelectromagnetic origin), which is equivalent to the vanishing of the normal component of the current at the interface, is physically related to the possibility of having a nonzero volume charge density at the surface [31,32]. The pressure term appearing in the hydrodynamic equation (see below) induces a smearing out of the charge density on the scale of the plasma screening length (given in our case by the Thomas-Fermi wavelength) [33], preventing the fluid from having singular behaviors at the surface. The influence of the resulting electron spill out at the particle surface has previously been studied by Toscano *et al.* [13] in a framework similar to the one employed here.

The nonlinear, nonlocal, and fully retarded version of the hydrodynamic model is described by the following equations [17]:

$$\partial_t n = -\boldsymbol{\nabla} \cdot (n\mathbf{v}), \tag{17a}$$

$$n\partial_t \mathbf{v} = -n(\mathbf{v} \cdot \boldsymbol{\nabla})\mathbf{v} - \frac{1}{M}\boldsymbol{\nabla} p - \gamma n\mathbf{v}$$
$$+ \frac{e}{M}n(\mathbf{E} + \mu_0 \mathbf{v} \times \mathbf{H}), \tag{17b}$$

where $M = 0.96m_e$ (m_e is the free-electron mass [24]), $n = n(\mathbf{r},t)$, $\mathbf{v} = \mathbf{v}(\mathbf{r},t)$, and $p = p(\mathbf{r},t)$ denote the electron fluid density, velocity, and pressure, respectively. Equations (17) are conservation relations addressing the number of charge carriers [Eq. (17a)] and their total momentum [Eq. (17b)]. They have been applied in different circumstances to describe the dynamics of carriers not only in metals but also semiconductors [34,35]. For metals, using the Thomas-Fermi approximation, the pressure is given as

$$p = \frac{1}{5}\frac{\hbar^2}{m_e}(3\pi^2)^{2/3}n^{5/3}. \tag{18}$$

Upon linearization, the above set of equations for the longitudinal component gives the usual nonlocal permittivity

$$\epsilon_{\text{L}}(\mathbf{k},\omega) = 1 - \frac{\omega_p^2}{\omega(\omega + i\omega\gamma) - \beta^2 k^2}, \tag{19}$$

while the transverse permittivity $\epsilon_{\text{T}}(\omega)$ still has the local form of Eq. (1). For our set of parameters we have $\beta^2 \approx 6.9738 \times 10^{11}\,\text{m}^2/\text{s}^2$. Owing to its simplicity, the linearized model allows for an analytical solution of the full electromagnetic problem in certain simple geometries. This is the case for a single-cylinder configuration, which has been used as an analytical reference for the convergence study of our numerical computations [17]. In the following, the DGTD method is used to solve the full nonlinear and nonlocal electromagnetic problem and to compute the scattering spectra of the dimer system. To calculate the spectra, a total-field/scattered-field (TFSF) formalism is employed, wherein a closed contour

is provided around the scatterer. At this contour a pulse is injected, and the scattering signal is subsequently calculated by recording the flux of the Poynting vector through said contour [22,30]. At first, the system is excited using a spectrally broadband Gaussian pulse with a central frequency of $0.67\omega_p$, a width of $1.36\,\omega_p$, and a rather low field amplitude of 10^3 V/m. The **E** field is polarized in plane, and we study two angles of incidence: incidence perpendicular to the dimer axis (**k** in the y direction) and along the dimer axis (**k** in the x direction).

In Fig. 5, we display the scattering spectra, calculated using both a nonlocal hydrodynamic Drude model and a local Drude model, while indicating the analytic quasielectrostatic solutions by vertical lines [36]. The corresponding spectra for both the local and nonlocal calculations exhibit clearly separated peaks which allow for classification by identifying them with the quasielectrostatic solutions for the different symmetry classes and different values of m (see Sec. II). The nonlocal spectra exhibit a blueshift with respect to the local calculations, which is a typical feature of the nonlocal material model in conjunction with hard-wall boundary conditions [37].

In Fig. 5(a), we display the spectra for an incident pulse propagating along the dimer axis. As expected from our group-theoretical analysis, for incidence along the dimer axis, all modes should be either class I or class III and therefore lie below the plasmon frequency. In fact, the fields belonging to the prominent peaks can be identified as belonging to class III. Modes of class I are, however, also allowed. Within the quasielectrostatic description, they are degenerate with those of class III and are therefore not visible in the scattering spectrum. In the Supplemental Material [29], we show that the modes of class I are, in fact, also excited and that in a fully retarded computation the degeneracy in frequency is lifted.

For incidence along the dimer axis [Fig. 5(b)], we have solutions of classes I and II, which energetically lie below and above the surface plasmon frequency, respectively. This also confirms the expectations from our group-theoretical considerations above [38]. For incidence along the dimer axis, we observe another notable effect of the nonlocality: The spectra show a number of small but well-separated peaks just above the surface plasmon frequency ω_{sp} which do not exist in the local case. They originate from high-order modes which, in a local description, coalesce at the limiting point ω_{sp} but, within a nonlocal framework, split away and are increasingly blueshifted beyond this frequency, separating from each other [11].

As a next step, we investigate the nonlinear properties of our model. As in Ref. [17], we raster scan a broad frequency range by exciting the system with spectrally narrowband Gaussian pulses (each with a spectral width of $0.03\omega_p$ and a field strength of 10^6 V/m) that are centered at different fundamental frequencies and subsequently record the second-harmonic signal once again employing the TFSF formalism. Specifically, the excitation pulses at the fundamental frequencies have to be chosen to exhibit a sufficiently narrow bandwidth such that their spectra have zero overlap with the second-harmonic frequency range, thereby enabling a background-free detection of the second-harmonic signal. In Fig. 6, we display the resulting second-harmonic spectra (the signal at the fundamental frequency of the excitation is *not* displayed;
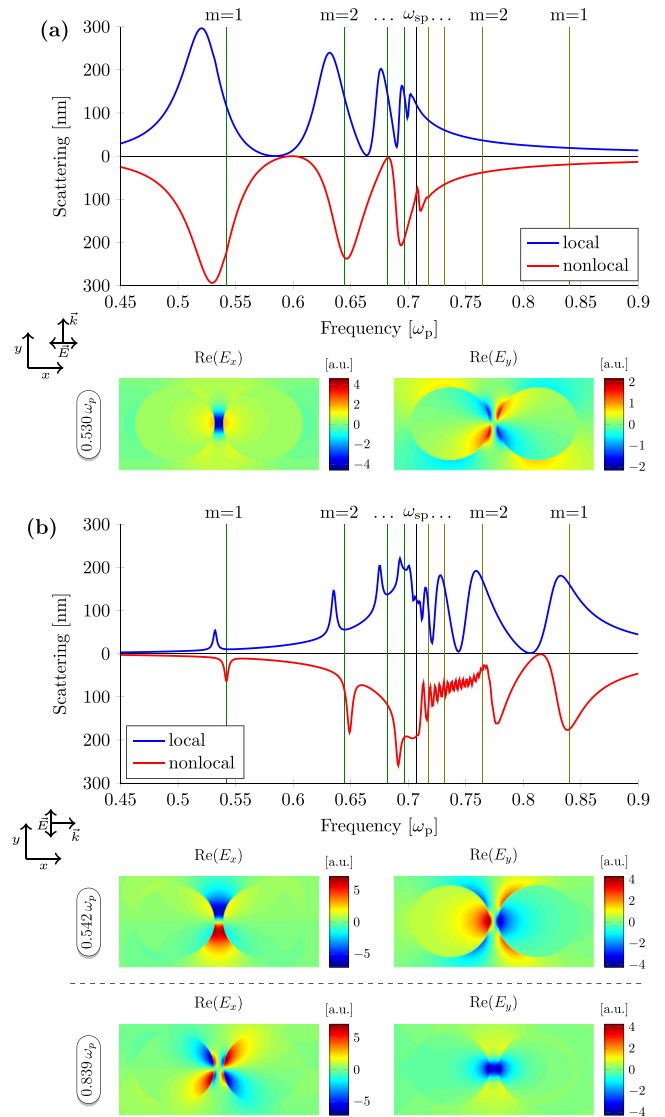

FIG. 5. The local and nonlocal spectra for a dimer structure for (a) incidence perpendicular to the dimer axis and (b) incidence along the dimer axis. The nonlocality has a particularly strong effect for the case in (b). For the local Drude model, the spectrum in (a) contains exclusively modes of class I or III that are confined to frequencies below the surface plasmon frequency ω_{sp} [as expected from (quasi)electrostatic theory]. For the nonlocal hydrodynamic Drude model, the entire spectrum is blueshifted. The field distributions were recorded at the frequencies corresponding to the $m = 1$ resonances and can be identified with the (quasi)electrostatic solutions from Fig. 3. The positions of the quasielectrostatic modes, according to Eq. (16), are indicated by vertical lines. Only the real part of the field distributions is displayed. The imaginary part can be found in the Supplemental Material [29].

it matches the linear spectrum known from the broadband calculations above). The corresponding SHG peaks can once again be associated with certain well-defined m values of the quasielectrostatic theory. For both excitation directions, we find a strong signal near $0.85\omega_p$, which corresponds to an $m = 1$ mode. Through the field distributions, we determine that the excitation, for both angles of incidence, belongs to
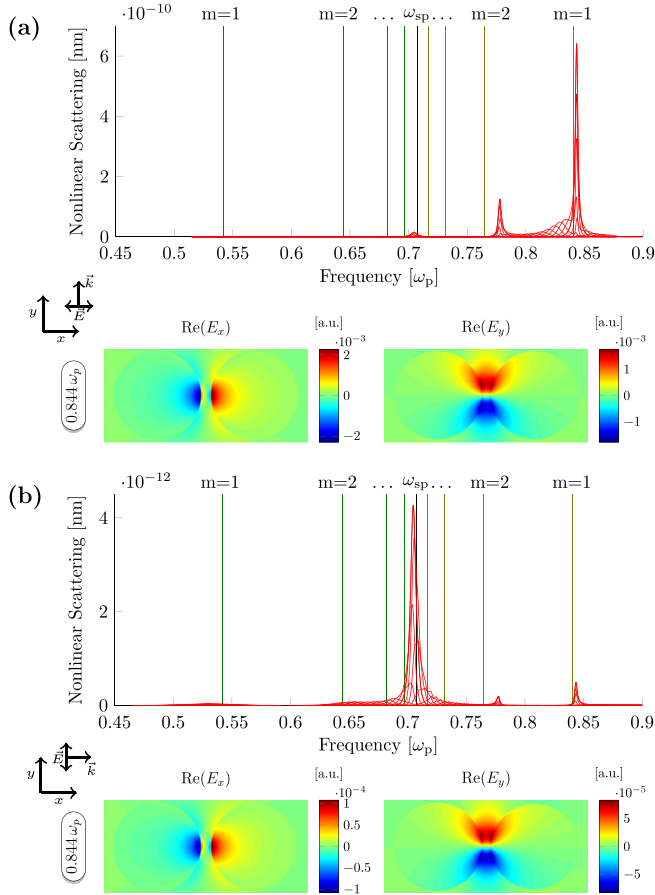
FIG. 6. Second-harmonic signals for (a) incidence perpendicular and (b) incidence along the dimer axis, obtained via a scan using a sequence of spectrally narrowband pulses at the fundamental frequencies. The field distributions are displayed for the $m = 1$ mode. The vertical lines indicate the positions of the quasielectrostatic modes [see Eq. (16)].

symmetry class IV, which cannot be excited on the linear level from the far field. Furthermore, for an excitation propagating perpendicular to the dimer axis [Fig. 6(a)], only resonances above the surface plasmon frequency ω_{sp} occur. There is a broad resonance just below the class IV $m = 1$ mode. This broad peak corresponds the class II $m = 1$ mode.

For an incident pulse along the dimer axis [Fig. 6(b)], there are resonances below and above the surface plasmon frequency ω_{sp}. An inspection of the field distributions shows that they belong to class III. This means that for both angles of incidence, we are now exciting those modes that were previously not excited in the linear calculations.

A group-theoretical investigation of the intrinsic symmetries of the hydrodynamic Drude model in combination with the Maxwell equations provides an explanation for this behavior. In order to facilitate our analysis, we treat the combined nonlinear set of equations within a perturbative approach. Specifically, the fields pertaining to the hydrodynamic equations are expanded into a series of harmonics [1,18],

$$\mathbf{E} = \mathbf{E}_0 + \mathbf{E}_1 + \mathbf{E}_1 + \cdots, \tag{20}$$

$$\mathbf{H} = \mathbf{H}_1 + \mathbf{H}_2 + \cdots, \tag{21}$$

$$n = n_0 + n_1 + n_2 + \cdots, \tag{22}$$

$$\mathbf{v} = \mathbf{v}_1 + \mathbf{v}_2 + \cdots, \tag{23}$$

where the subscripts $i = 0, 1, 2$ correspond to static fields, fields at the fundamental frequencies, and fields pertaining to the second-order response, respectively. Upon inserting the above expansions into the hydrodynamic equations (17), we obtain source distributions for the fields at the second-order response that are expressed in terms of various combinations of the fields at the fundamental frequency. Consequently, we can determine the symmetry properties of the second-order fields from the symmetries of the corresponding source distributions, i.e., from the symmetries of the fundamental fields through appropriate compatibility relations (see the Supplemental Material [29]). Using this procedure, we find

$$\mathcal{T}[E_{2x}] = B_2[\mathcal{T}[E_{1x}]]^2. \tag{24}$$

We recall that for a wave packet propagating in the y direction, the symmetry of the incoming electric field is given by

$$\mathcal{T}\big[E_{x,\text{inc}}^{k_y}\big] = \mathcal{T}[E_{1x}] = A \oplus B_3, \tag{25}$$

which is compatible with modes of classes I and II that are both excited in this case. Calculating the second-order fields

$$\mathcal{T}\big[E_{2x}^{k_y}\big] = B_2[A \oplus B_3]^2 = B_2(A \oplus B_3) = B_2 \oplus B_1 \tag{26}$$

reveals that the second-harmonic modes are associated with the remaining two symmetries, i.e., the modes of classes II and IV (see Fig. 3). We thus explicitly see that the transformation behavior of the second-order fields differs from that of the fundamental (excitation) fields, thus explaining many nontrivial features of SHG spectra. The considerations on the incidence of a pulse propagating in the x direction proceed in a completely analogous fashion. Starting with

$$\mathcal{T}\big[E_{y,\text{inc}}^{k_x}\big] = A \oplus B_2, \tag{27}$$

the modes of classes I and II are excited, which must have first-order E_x fields of the type

$$\mathcal{T}\big[E_{1x}^{k_x}\big] = B_1 \oplus B_3. \tag{28}$$

Therefore, for the second-order response, we find

$$\mathcal{T}\big[E_{2x}^{k_x}\big] = B_2[B_1 \oplus B_3]^2 = B_2(A \oplus B_2) = B_2 \oplus A, \tag{29}$$

which means that second harmonics of classes III and IV are excited (see Fig. 3).

B. V-groove

The findings from the previous section can be applied to other systems with different symmetry. For instance, a V-groove structure, i.e., a rod-shaped antenna with a notch on one side (see Fig. 7) represents a system with a lower symmetry than that of a dimer as it cannot be mirrored upside down. In a recent work we found that this system exhibits strong second-harmonic generation efficiencies due to the possibility to engineer the structure to exhibit double-resonant effects [17].

In fact, the V-groove exhibits a symmetry corresponding to the point group C_2. It is mapped onto itself by a rotation around the y axis (which in two dimensions is isomorphic to mirroring
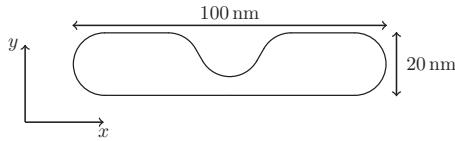
FIG. 7. Schematic of the V-groove geometry, including geometric data.

on the yz plane). Since C_2 represents a subgroup of the D_2 group of the dimer, we can simply reuse the group-theoretical analysis developed for the dimer and adapt it to the V-groove case. This means that, to obtain the character table of C_2, the operations not belonging to this point group can be eliminated from the character table of D_2 (see Table II). Consequently, only two symmetries and two classes of modes, hereafter called I′ and II′, remain, and we can identify the symmetries of the dimer geometry with those of the V-groove geometry as

$$B_1^{D_2} \equiv B^{C_2}, \tag{30}$$

$$B_2^{D_2} \equiv B^{C_2}, \tag{31}$$

$$A^{D_2} \equiv A^{C_2}, \tag{32}$$

$$B_3^{D_2} \equiv A^{C_2}. \tag{33}$$

By carrying out the corresponding substitutions in the equations for the dimer, we readily obtain the symmetries for the first- and second-order fields for the V-groove. Specifically, for a wave propagating in the y direction, with the $\mathbf{E}$ field polarized in the x direction, we find

$$\mathcal{T}\big[E_{1x,\text{dimer}}^{k_y}\big] = A^{D_2} \oplus B_3^{D_2}$$

$$\longrightarrow \quad \mathcal{T}\big[E_{1x,\text{V-groove}}^{k_y}\big] = A^{C_2}, \tag{34}$$

and therefore, the second-order field is given by

$$\mathcal{T}\big[E_{2x,\text{V-groove}}^{k_y}\big] = B^{C_2}[A^{C_2}]^2$$

$$= B^{C_2}(A^{C_2})$$

$$= B^{C_2}. \tag{35}$$

This demonstrates that, for this direction of incidence, the nonlinearly excited modes are different from those that are excited in the linear limit.

For pulses with the direction of incidence along the x axis, we find for the mode symmetries

$$\mathcal{T}\big[E_{1x,\text{dimer}}^{k_x}\big] = B_1^{D_2} \oplus B_3^{D_2}$$

$$\longrightarrow \quad \mathcal{T}\big[E_{1x,\text{V-groove}}^{k_x}\big] = B^{C_2} \oplus A^{C_2}, \tag{36}$$

TABLE II. Character table of the point group C_2. Since C_2 is a subgroup of D_2, the corresponding character table can be obtained by deleting some operations (indicated by a dash) of Table I.

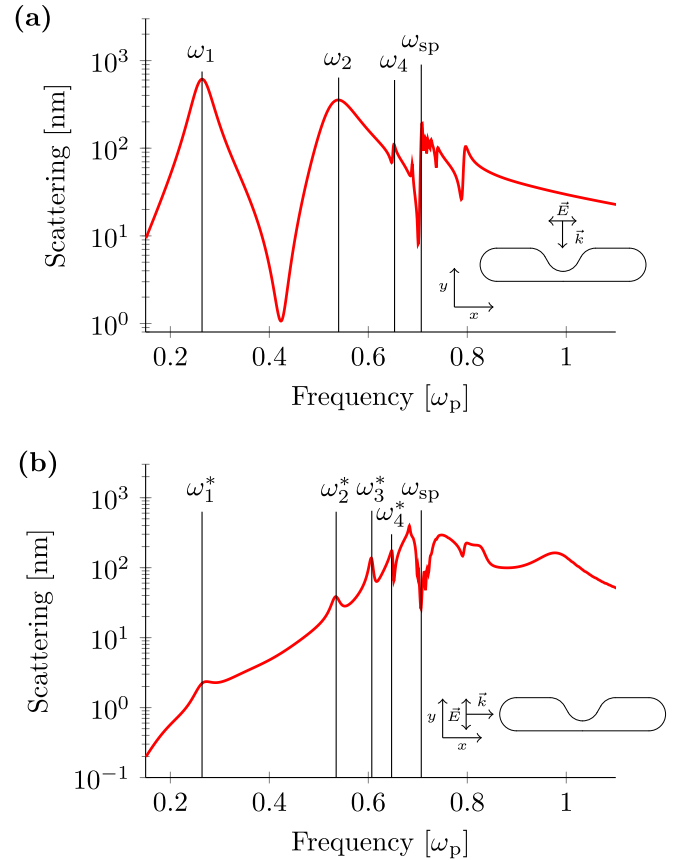| C_2	I	$C_2(z)$	σ_{xz}	σ_{yz}
A	1	—	—	1
B_1	1	—	—	−1
$B_2 = B_1$	1	—	—	−1
$B_3 = A$	1	—	—	1

FIG. 8. Linear scattering spectra for the V-groove structure. (a) Incidence along the short axis. (b) Incidence along the long axis. The resonances indicated by vertical lines will be important in the discussion of SHG (see Fig. 9). The plots employ a logarithmic scale on the y axis.

so that modes of both symmetry classes can be excited. For the second-order fields, we obtain

$$\mathcal{T}\big[E_{2x,\text{V-groove}}^{k_x}\big] = B^{C_2}[B^{C_2} \oplus A^{C_2}]^2$$

$$= B^{C_2}(A^{C_2} \oplus B^{C_2})$$

$$= B^{C_2} \oplus A^{C_2}, \tag{37}$$

which demonstrates that both classes of modes can also be excited at the second-order response.

We are now in a position to computationally validate the symmetry relations at both the linear and second-order response levels. In addition, we can classify the symmetries of the excited modes by close inspection of the corresponding linear and second-order scattering spectra. In other words, contrary to the standard approach where the symmetry of the excited modes allows for assessing the second-order response, we have, based on our group-theoretical analysis, sufficient information to invert the procedure and determine the excited modes just by analyzing the linear and nonlinear spectra.

To demonstrate this, we again use a broadband excitation pulse to compute the linear scattering spectra (see Fig. 8). According to the symmetry analysis, for incidence with the $\mathbf{E}$ field polarized in the x direction and the k vector pointing along the y axis (*short* axis), only one class of modes (class I′)
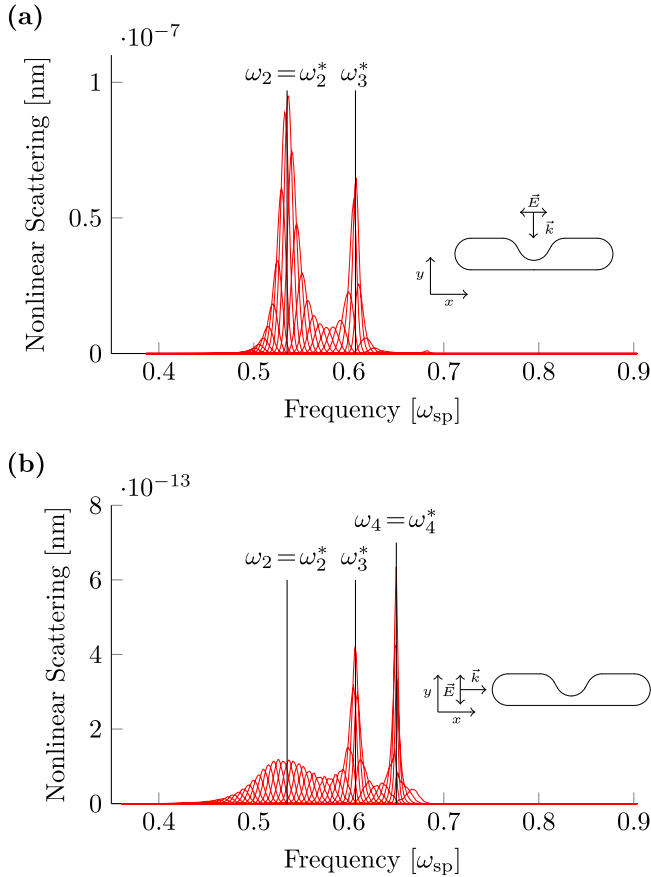
FIG. 9. Second-harmonic spectra from a doubly resonant V-groove. (a) Incidence along the short axis. A strong doubly resonant behavior is found as the linear signal coincides with ω_1, yielding a signal that is five orders of magnitude larger than for the other angle of incidence [17]. Resonances are found at the frequencies of $\omega_2 = \omega_2^*$ and of ω_3^*. (b) Incidence along the long axis. A doubly resonant enhancement is not found as the ω_1^* resonance on the linear level is weak for this direction of incidence. Resonances are found at the frequencies of $\omega_2 = \omega_2^*$, of ω_3^*, and of $\omega_4 = \omega_4^*$. Note that the linear signal is scanned across only the ω_1 peak, from $0.25\omega_p$ to $0.35\omega_p$, where doubly resonant behavior is expected. This is not a frequency scan over the whole spectrum.

is excited. Thus, all modes in Fig. 8(a), labeled ω_1, ω_2, and ω_4, must belong to this class. If the direction of incidence is rotated by $90°$ (*long* axis), both class I′ and II′ modes are excited. The latter spectrum is displayed in Fig. 8(b), and all resonances for the corresponding direction of incidence $\omega_1^*, \omega_2^*,$ ω_3^*, and ω_4^* are marked by an asterisk for later reference. A close inspection of the spectra in Fig. 8 reveals that for every frequency at which there is a resonance in Fig. 8(a), there is also a resonance in Fig. 8(b), but the reverse does not hold. This is fully consistent with the group-theoretical analysis which suggests that, for incidence along the long axis, both classes of modes are excited, while for incidence along the short axis only one class is excited [see Eqs. (34) and (36)]. All peaks in the spectra of Fig. 8(a) must pertain to class I′. Three peaks which will be important for our subsequent discussions are labeled ω_1, ω_2, and ω_4. On the other hand, the peaks in Fig. 8(b) could correspond to either class I′ or class II′ modes. We find that

TABLE III. Summary of the symmetry classes of the modes excited in the V-groove geometry. The asterisk indicates that, in the linear spectrum, the spectral peak was found during excitation along the long axis of the structure. Peaks ω_2 and ω_2^* are degenerate in frequency. While ω_2 has contributions from only class I′, ω_2^* has contributions from both classes. Peak ω_3^*, which was found for only one excitation direction, is class II′. Peaks ω_4 and ω_4^* come from the same mode, which is class I′. The fundamental signal for this SHG study was chosen near ω_1 to exploit the doubly resonant behavior of the structure; hence, the peak at ω_1 itself is excluded from the study.

	ω_2	ω_2^*	ω_3^*	ω_4	ω_4^*
Class I′	X	X		X	X
Class II′		X	X		

the peaks labeled ω_1^*, ω_2^*, and ω_4^* occur at the same frequencies ω_1, ω_2, and ω_4 as before. Therefore, each of these peaks could have contributions of a class I′ mode and a class II′ mode. The peak labeled ω_3^* can have only contributions from class II′ since no peak is found at this frequency when the system is excited along the short axis [Fig. 8(b)]. By investigating the second-order response, the contributions to peaks ω_1^*, ω_2^*, and ω_4^* can be identified.

According to Eq. (24), for the second-order response, for incidence along the short axis, the nonlinearly excited modes are class II′, i.e., precisely those modes that are not excited by the fundamental signal. In turn, for incidence along the long axis, on both the fundamental (linear) and second-order (nonlinear) levels, modes of classes I′ and II′ will be excited.

In Fig. 9, we display the SHG spectra for the V-groove structure, just like before for the dimer in Fig. 6. We notice first that the frequencies ω_2^*, ω_3^*, and ω_4^* are such that they are approximately at twice the frequency of ω_1^*. Thus, utilizing a fundamental pulse centered near ω_1^* that generates a second-harmonic signal at those peaks leads to a doubly resonant excitation. Note that since the fundamental signal is centered near ω_1^*, the peak at ω_1^* itself is not included in the SHG studies. For incidence along the short axis, the fundamental signal at ω_1 is very strong, which yields a strong double resonance, while for incidence along the long axis, the signal (ω_1^*) is very small, and therefore, the double-resonance effect is weak (see Fig. 9). For incidence along the short axis, there is a strong SHG enhancement, yielding a signal which is approximately five orders of magnitude larger than the signal obtained for incidence along the long axis.

As pointed out above, an analysis of the SHG spectra in Fig. 9 suffices to determine whether the peaks under investigation pertain to class I′ or class II′ (see Table III for a summary). In fact, two very pronounced peaks at frequencies ω_2^* and ω_3^* are found in Fig. 9(a). Above, we already discussed that the class II′ ω_3^* mode is expected in the SHG signal. The fact that there is also a resonance at ω_2^* means that the ω_2^* peak in the linear spectrum must have a contribution of a class II′ mode which is degenerate in frequency with the ω_2 class I′ mode. On the other hand, the fact that there is no SHG signal at ω_4^* means that the ω_4^* has only a class I′ contribution, just like ω_4. The SHG signal for incidence along the long axis [Fig. 9(b)] exhibits peaks at all three frequencies, ω_2^*, ω_3^*, and

ω_4^*. This confirms the group-theoretical prediction that, for this direction of incidence, modes from both symmetry classes are excited linearly and nonlinearly. Consequently, the mode at ω_3^*, which is clearly class II′, is excited linearly and nonlinearly, and so is peak ω_4, which, in turn, we have identified as having class I′ contributions. Finally, peak ω_2^* is a mixed result of the class I′ and class II′ modes' responses at this same frequency.

IV. CONCLUSIONS

We have presented a numerical and analytical study of the plasmonic modes in different nanowire systems and their excitation on both the fundamental linear and second-order nonlinear levels. A description based on the quasielectrostatic approximation allows for an extremely useful mode classification which, for cylindrical dimer systems and the ordinary Drude model, has been carried out fully analytically. In combination with a group-theoretical analysis of the fundamental linear and second-order nonlinear responses, we have established mode selection rules predicting the excitation of the linear and nonlinear plasmonic modes for different directions of incidence. With the help of the analytical results, we have been able to interpret the resulting linear and nonlinear numerical spectra obtained using the DGTD method, although the computations were performed outside the quasielectrostatic regime and using a nonlocal material model. In order to further demonstrate the utility of the mode classification and group-theoretical analyses, we have derived the selection rules of a low-symmetry single V-groove system from those of the high-symmetry dimer system. This also shows that our analyses can be readily applied to other geometries which have a symmetry that is the same as or lower than that of a cylindrical dimer, i.e., a very wide range of possible nanoantenna geometries.

Our analysis relies on the nonlocal, nonlinear, and fully retarded hydrodynamic Drude model as described in Eqs. (17). In such a model the metal is described as a plasma with finite compressibility, in contrast to a local description where the fluid is rigid. The hydrodynamic equations allow for the analytical inspections and numerical implementations presented above and provide a good description of the system. Further investigations will aim to improve such a description by considering further effects such as the Landau damping, which were neglected in our present treatment. Previous work [39] has indeed shown that the interplay between nonlocality and dissipation can substantially alter some features of the resonance spectrum, adding, for example, additional line broadening. Modifications of the hydrodynamic model which partially take these features into account have already been presented in the literature [2,3,10,13,13,14,40]. Further, by exploiting the connection to plasma physics, an alternative and highly interesting procedure relies on the implementation of the fully nonlinear Boltzmann transport equation to describe the dynamics of the carrier (quantum) distribution in the metal [33,41]. The combination of this and other similar approaches, providing a microscopically based description of the material properties, with an analysis of the geometry-induced system symmetries offers a powerful and constructive route for designing realistic and highly efficient nanodevices that are able to achieve strong SHG.

[1] J. E. Sipe, V. C. Y. So, M. Fukui, and G. I. Stegeman, Analysis of second-harmonic generation at metal surfaces, Phys. Rev. B **21**, 4389 (1980).

[2] A. Liebsch, Surface-plasmon dispersion and size dependence of Mie resonance: Silver versus simple metals, Phys. Rev. B **48**, 11317 (1993).

[3] P. Halevi, Hydrodynamic model for the degenerate free-electron gas: Generalization to arbitrary frequencies, Phys. Rev. B **51**, 7497 (1995).

[4] F. J. García de Abajo, Nonlocal effects in the plasmons of strongly interacting nanoparticles, dimers, and waveguides, J. Phys. Chem. C **112**, 17983 (2008).

[5] I. Villó-Pérez and N. R. Arista, Hydrodynamical model for bulk and surface plasmons in cylindrical wires, Surf. Sci. **603**, 1 (2009).

[6] C. Cirací, E. Poutrina, M. Scalora, and D. R. Smith, Origin of second-harmonic generation enhancement in optical split-ring resonators, Phys. Rev. B **85**, 201403 (2012).

[7] C. Cirací, E. Poutrina, M. Scalora, and D. R. Smith, Second-harmonic generation in metallic nanoparticles: Clarification of the role of the surface, Phys. Rev. B **86**, 115451 (2012).

[8] L. Stella, P. Zhang, F. J. García-Vidal, A. Rubio, and P. García-González, Performance of nonlocal optics when applied to plasmonic nanostructures, J. Phys. Chem. C **117**, 8941 (2013).

[9] C. Cirací, J. B. Pendry, and D. R. Smith, Hydrodynamic model for plasmonics: A macroscopic approach to a microscopic problem, Chem. Phys. Chem. **14**, 1109 (2013).

[10] N. A. Mortensen, S. Raza, M. Wubs, T. Søndergaard, and S. I. Bozhevolnyi, A generalized non-local optical response theory for plasmonic nanostructures, Nat. Commun. **5**, 3809 (2014).

[11] T. Christensen, W. Yan, S. Raza, A.-P. Jauho, N. A. Mortensen, and M. Wubs, Nonlocal response of metallic nanospheres probed by light, electrons, and atoms, ACS Nano **8**, 1745 (2014).

[12] S. Raza, S. I. Bozhevolnyi, M. Wubs, and N. A. Mortensen, Nonlocal optical response in metallic nanostructures, J. Phys. Condens. Matter **27**, 183204 (2015).

[13] G. Toscano, J. Straubel, A. Kwiatkowski, C. Rockstuhl, F. Evers, H. Xu, N. A. Mortensen, and M. Wubs, Resonance shifts and spill-out effects in self-consistent hydrodynamic nanoplasmonics, Nat. Commun. **6**, 7132 (2015).

[14] C. Ciracì and F. Della Sala, Quantum hydrodynamic theory for plasmonics: Impact of the electron density tail, Phys. Rev. B **93**, 205405 (2016).

[15] M. Scalora, M. A. Vincenti, D. de Ceglia, V. Roppo, M. Centini, N. Akozbek, and M. J. Bloemer, Second- and third-harmonic generation in metal-based structures, Phys. Rev. A **82**, 043828 (2010).

[16] Y. Zeng, W. Hoyer, J. Liu, S. W. Koch, and J. V. Moloney, Classical theory for second-harmonic generation from metallic nanoparticles, Phys. Rev. B **79**, 235109 (2009).

[17] A. Hille *et al.*, Second harmonic generation from metal nano-particle resonators: Numerical analysis on the basis of the hydrodynamic drude model, J. Phys. Chem. C **120**, 1163 (2016).

[18] D.-N. Huynh, M. Moeferdt, C. Matyssek, C. Wolff, and K. Busch, Ultrafast three-wave-mixing in plasmonic nanostructures, Appl. Phys. B **122**, 139 (2016).

[19] G. Toscano, S. Raza, S. Xiao, M. Wubs, A.-P. Jauho, S. I. Bozhevolnyi, and N. A. Mortensen, Surface-enhanced Raman spectroscopy: Nonlocal limitations, Opt. Lett. **37**, 2538 (2012).

[20] G. Toscano, S. Raza, A.-P. Jauho, N. A. Mortensen, and M. Wubs, Modified field enhancement and extinction by plasmonic nanowire dimers due to nonlocal response, Opt. Express **20**, 4176 (2012).

[21] P. Ginzburg, A. V. Krasavin, G. A. Wurtz, and A. V. Zayats, Nonperturbative hydrodynamic model for multiple harmonics generation in metallic nanostructures, ACS Photonics **2**, 8 (2014).

[22] K. Busch, M. König, and J. Niegemann, Discontinuous Galerkin methods in nanophotonics, Laser Photonics Rev. **5**, 773 (2011).

[23] N. Schmitt, C. Scheid, S. Lanteri, A. Moreau, and J. Viquerat, A DGTD method for the numerical modeling of the interaction of light with nanometer scale metallic structures taking into account non-local dispersion effects, J. Comput. Phys. **316**, 396 (2016).

[24] P. B. Johnson and R. W. Christy, Optical Constants of the Noble Metals, Phys. Rev. B **6**, 4370 (1972).

[25] P. Lucht, Bipolar Coordinates and the Two-Cylinder Capacitor, http://user.xmission.com/~rimrock/, 2015.

[26] R. Ruppin, Optical absorption of two spheres, J. Phys. Soc. Jpn. **58**, 1446 (1989).

[27] A. I. Luo, Y. Fernandez-Dominguez, A. Wiener, S. A. Maier, and J. B. Pendry, Surface Plasmons and Nonlocality: A Simple Model, Phys. Rev. Lett. **111**, 093901 (2013).

[28] K.-H. Gericke, Charakterentabelle für chemisch wichtige Punktgruppen, http://www.pci.tu-bs.de/aggericke/PC2/Punktgruppen/Punktgruppen.htm.

[29] See Supplemental Material at http://link.aps.org/supplemental/10.1103/PhysRevB.97.075431 for additional spectra and field distributions as well as for more information about the symmetry properties of the system.

[30] J. S. Hesthaven and T. Warburton, *Nodal Discontinuous Galerkin Methods: Algorithms, Analysis, and Applications* (Springer, New York, 2007).

[31] P. Jewsbury, Electrodynamic boundary conditions at metal interfaces, J. Phys. F **11**, 195 (1981).

[32] G. W. Ford and W. H. Weber, Electromagnetic interactions of molecules with metal surfaces, Phys. Rep. **113**, 195 (1984).

[33] G. Manfredi, How to model quantum plasmas, Fields Inst. Commun. **46**, 263 (2005).

[34] M. Sumi, Traveling-wave amplification by drifting carriers in semiconductors, Jpn. J. Appl. Phys. **6**, 688 (1967).

[35] J. Thiennot, Les ondes de charge d'espace dans les semiconducteurs et l'amplificateur a onde progressive à l'état solide, J. Phys. (Paris) **33**, 219 (1972).

[36] Since the calculations are done for a two-dimensional, i.e., infinitely extended, structure along the z axis, scattering takes on the one-dimensional unit nanometers, which is to be interpreted as nanometers per unit length along the z axis.

[37] R. Ruppin, Extinction properties of thin metallic nanowires, Opt. Commun. **190**, 205 (2001).

[38] For this case, we have confirmed that for very small structures ($r \approx 1$ nm), the quasielectrostatic limit is approached and the solutions of class I are strongly suppressed.

[39] F. Intravaia and K. Busch, Fluorescence in nonlocal dissipative periodic structures, Phys. Rev. A **91**, 053836 (2015).

[40] S. Raza, T. Christensen, M. Wubs, S. I. Bozhevolnyi, and N. A. Mortensen, Nonlocal response in thin-film waveguides: Loss versus nonlocality and breaking of complementarity, Phys. Rev. B **88**, 115401 (2013).

[41] J. A. Bittencourt, *Fundamentals of Plasma Physics* (Springer, New York, 2013).